

Constraints in 3D gravity inversion

Olivier Boulanger* and Michel Chouteaut†

Ecole Polytechnique de Montréal, Montréal Qc., H3C 3A7, Canada

Received July 1999, revision accepted October 2000

ABSTRACT

A three-dimensional (3D) inversion program is developed to interpret gravity data using a selection of constraints. This selection includes minimum distance, flatness, smoothness and compactness constraints, which can be combined using a Lagrangian formulation. A multigrid technique is also implemented to resolve separately large and short gravity wavelengths. The subsurface in the survey area is divided into rectangular prismatic blocks and the problem is solved by calculating the model parameters, i.e. the densities of each block. Weights are given to each block depending on depth, *a priori* information on density and the density range allowed for the region under investigation. The present computer code is tested on modelled data for a dipping dike and multiple bodies. Results combining different constraints and a weight depending on depth are shown for the dipping dike. The advantages and behaviour of each method are compared in the 3D reconstruction. Recovery of geometry (depth, size) and density distribution of the original model is dependent on the set of constraints used. From experimentation, the best combination of constraints for multiple bodies seems to be flatness and a minimum volume for the multiple bodies. The inversion method is tested on real gravity data from the Rouyn-Noranda (Quebec) mining camp. The 3D inversion model for the first 10 km is in agreement with the known major lithological contacts at the surface; it enables the determination of the geometry of plutons and intrusive rocks at depth.

INTRODUCTION

The goal of inverse theory is to determine model parameters from observations. Although a solution that satisfies the observed data can easily be found, its non-uniqueness in potential methods is caused by the nature of the physics and the under-determination of the problem. To deal with non-uniqueness using models composed of a large number of contiguous cells of unknown density, many authors add *a priori* information to constrain the solution. Green (1975) used an appropriate weighting matrix to fix some of the parameters when geological or density information was available. Others authors (Li and Oldenburg 1996, 1998;

Pilkington 1997) counteracted the decreasing sensitivity of cells with depth by weighting them with an inverse function of depth. Last and Kubik (1983) found a compact solution with a minimum volume constraint. Guillen and Menichetti (1984) and Barbosa and Silva (1994) concentrated the solution along inertial axes. A global constraint called ‘smoothing’ was used to find a model with a minimum structure (Djeridane 1996; Li and Oldenburg 1996).

In the following, we first propose an analytical calculation of the gravity anomaly derived from a cell model; it allows analysis of the symmetry of the sensitivity coefficients leading to minimization of the amount of memory storage. The behaviour of sensitivity is presented to help understand the convergence to a model in the inverse problem. A simple analytical relationship is developed from the sensitivity of a spherical cell to choose automatically the dimensions of

*E-mail: olivierb@geo.polymtl.ca

†E-mail: chouteau@geo.polymtl.ca

the model domain. Next, the inverse problem based on a Lagrangian formulation enables us to insert all equality constraints with a weighted norm cost function. The third and fourth parts are devoted to the solution of the Lagrangian formulation and to an application of the multigrid technique, respectively. Tests are performed using different combinations of constraints on modelled data. Finally, a test on real data from the mining camp of Rouyn-Noranda (Abitibi, Quebec) yields a density structure of the upper 10 km which is compared with the known geological information.

GRAVITY MODELLING

The purpose of forward modelling is to compute the gravimetric response g at the surface due to a density distribution in the subsurface. This calculated anomaly is compared with the observed anomaly g^{obs} in the survey area. For convenience we decided to discretize the subsurface as an ensemble of rectangular prisms (Fig. 1). This classic method can consume huge memory space for a large set of observations, however we use the symmetry of the kernel to minimize the amount of memory. Thus the attraction g at each surface station is due to the sum of the responses of each block. The solution for the gravitational attraction $g_i \equiv g(x_i, y_i, z_i)$ of a j th right rectangular prism with dimensions described by the limits $x'_1 \leq x' \leq x'_2$, $y'_1 \leq y' \leq y'_2$ and

$z'_1 \leq z' \leq z'_2$ using Cartesian coordinates is given by

$$g_i = -\gamma \rho_j \int_{x'_1}^{x'_2} dx' \int_{y'_1}^{y'_2} dy' \int_{z'_1}^{z'_2} dz' \times \frac{(z_i - z')}{((x_i - x')^2 + (y_i - y')^2 + (z_i - z')^2)^{3/2}}. \quad (1)$$

The density ρ_j is assumed to be constant within the prism. A solution of this integral was first developed by Haáz (1953) and was used by other authors (Nagy 1966; Banerjee and Gupta 1977; Bear, Al-Shukri and Rudman 1995). A synthetic development was made by Li and Chouteau (1998) and a proof is given for the validity of (2) when gravity is calculated outside, on the boundary and inside the prism. Equation (2) is

$$\frac{g_i}{\rho_j} = -\gamma \sum_{p=1}^2 \sum_{q=1}^2 \sum_{s=1}^2 \mu_{pqs} \times \left[a_p \ln(b_q + r_{pqs}) + b_q \ln(a_p + r_{pqs}) - c_s \arctan\left(\frac{a_p b_q}{c_s r_{pqs}}\right) \right], \quad (2)$$

where

- g_i is the gravitational attraction measured at point (x_i, y_i, z_i) ;
- ρ_j is the contrast of density for the j th prism;
- γ is the universal gravitational constant;
- $\mu_{pqs} = (-1)^p (-1)^q (-1)^s$ with $p, q, s = 1, 2$;
- $a_p = x_i - x'_p$, $b_q = y_i - y'_q$ and $c_s = z_i - z'_s$;

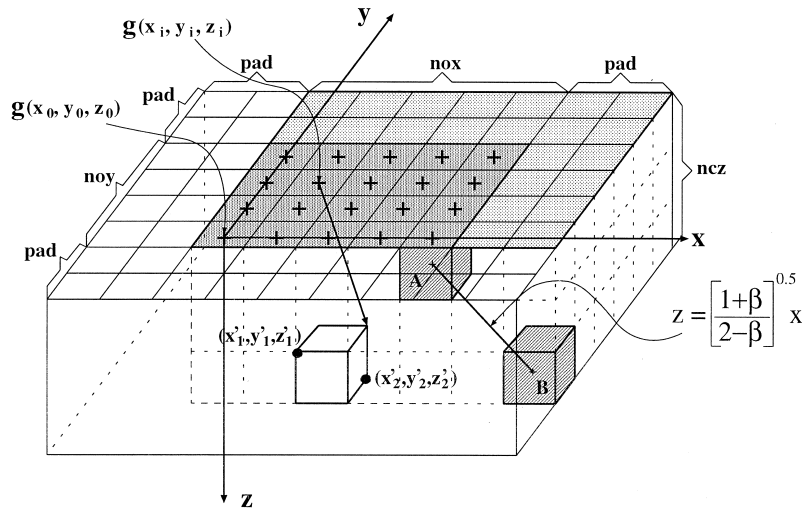


Figure 1 Discretization of the subsurface with prisms. Gravity stations $g(x_i, y_i, z_i)$ are located at the centre of the upper face of prisms in the top layer. The stations lie on a horizontal grid at a constant elevation $z_i (= z_0)$. Increments in the x -, y - and z -directions are δx , δy and δz . nox and noy are the number of observations in the x - and y -directions, respectively, and $ncx = nox + 2 \cdot pad$, $ncy = noy + 2 \cdot pad$ and ncz denote the number of cells in the x -, y - and z -directions. pad denotes the cells added around the domain of observation. The line linking cells A and B indicates the maximum sensitivity $G_{s,\beta}^{\text{MAX}}$. The grey zone delimits the domain above a minimum sensitivity, used to calculate the gravity data.

- (x'_p, y'_q, z'_s) are the coordinates of the eight corners of the j th prism;
- $r_{pqs} = (a_p^2 + b_q^2 + c_s^2)^{1/2}$ is the distance between one corner of the prism and the observation site (x_i, y_i, z_i) as shown in Fig. 1.

The term on the right-hand side of the equality is denoted by G_{ij} and is the kernel. This response is valid only at the station g_i and for one prism ρ_j . Gravity stations $g(x_i, y_i, z_i)$ are located at the centre of the upper face of prisms in the top layer with a constant elevation z_i depending on the observation points with regard to ground level (typically $z_i = z_0 = -0.1$ m). This is to take into account the actual height of the instrument above the ground. To obtain the total response at each station g_i ($i = 1, N$), we sum the gravity response of $M = ncx \times ncy \times ncz$ prisms:

$$g_i = \sum_{j=1}^M G_{ij} \rho_j. \quad (3)$$

In matrix notation we can write $\mathbf{g} = \mathbf{G}\boldsymbol{\rho}$, where \mathbf{G} is also called the sensitivity matrix relating the gravimetric acceleration \mathbf{g} and the contrast of density $\boldsymbol{\rho}$. To avoid an exponent in units, we use g/cm^3 ($\equiv 1000 \text{ kg/m}^3$) for the density contrast and mGal ($\equiv 10^{-5} \text{ m/s}^2$) for the gravitational attraction. In the next section, properties of the kernel are used to minimize memory storage and to determine the dimensions of the model domain using a simple analytical relationship.

SENSITIVITY MATRIX

The aim of this section is to show the symmetry and the behaviour of the kernel G when it is normalized by weighting coefficients. Finally, a relationship for determining the dimensions of our domain and a choice of cell size is proposed.

Symmetry and storage optimization

Figure 2 shows for one station g_i that the kernel is symmetric with respect to the vertical z -axis. This pattern is identical for all stations located at coordinates (x_i, y_i, z_i) . The product $G_{ij}\rho_j$ is just a spatial convolution of $G_{i,j}$ with the 3D density distribution ρ_j . Thus the model can be split into four quadrants using its symmetry to calculate only the sensitivity of the first quadrant (Fig. 2a). If we choose the coordinates (x_0, y_0, z_0) for the station g at the corner of the 2D data grid (see grey zone in Fig. 1), we need to calculate only the first row of the matrix \mathbf{G} (G_{1j} with $j = 1, M$). The rest of the elements of G_{ij} can be found using the appropriate value of j . In fact, we store G_{1j} in a 3D array $G(ig, jg, kg)$ where

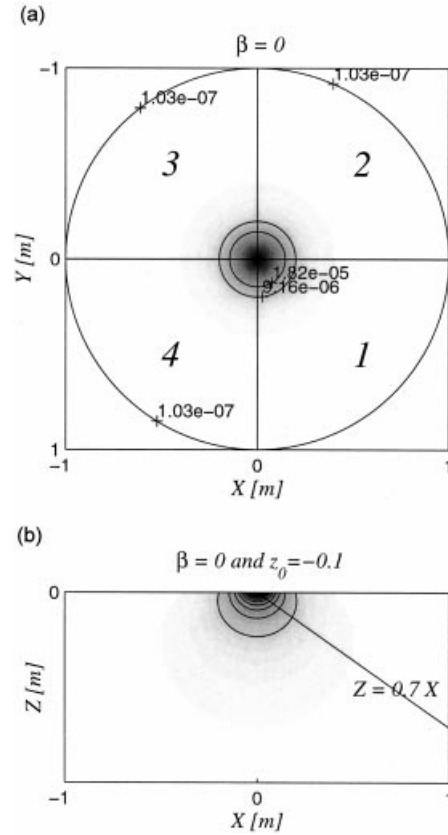


Figure 2 Normalized sensitivity coefficients G/γ for $\beta = 0$ and for a station located at $z_0 = -0.1$ m. (a) Plan view at the surface: numbers 1 to 4 delimit the four quadrants. (b) Section at $Y = 0$ m. Equation (6) giving maximum sensitivity for $\beta = 0$ is plotted as a dipping black line.

$ig = [1, nox + pad]$, $jg = [1, noy + pad]$ and $kg = [1, ncx]$. The indices associated with the observations are $io = [1, nox]$ and $jo = [1, noy]$ and with the parameters are $ip = [1, ncx]$, $jp = [1, ncy]$ and $kp = [1, ncx]$. Five nested loops operating on the jo, io, kp, jp, ip indices, respectively, are used to compute the sensitivity terms. These indices serve to determine, among other things, the indices $ig = |(ip - pad) - io| + 1$, $jg = |(jp - pad) - jo| + 1$ and $kg = kp$, which give the appropriate value of sensitivity. The amount of memory required to store $G(ig, jg, kg)$ is simply a $(1 \times M)$ vector with $M = (nox + pad) \times (noy + pad) \times ncx$, instead of an $(N \times M)$ matrix. pad denotes the number of cells of padding used to extend the model domain and is discussed in the next paragraph.

Weighting the sensitivity matrix

We now analyse the behaviour of the sensitivity G_{ij} , normalized

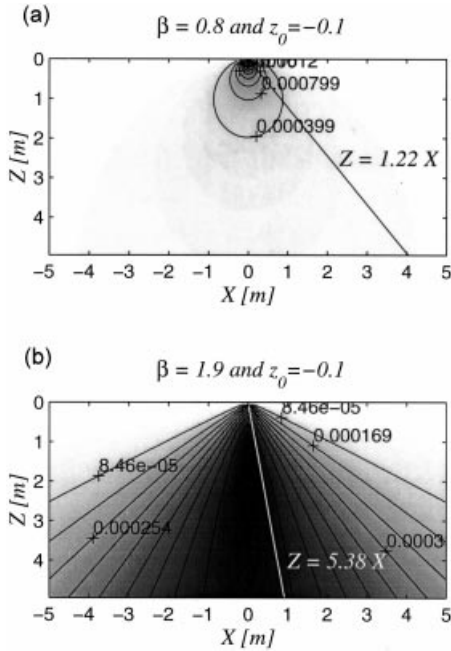


Figure 3 Section at $Y = 0$ m of the normalized sensitivity coefficients G/γ for a station located at $z_0 = -0.1$ m and for (a) $\beta = 0.8$ and (b) $\beta = 1.9$. Equation (6) for the selected β is plotted as a dipping line.

by the universal gravitational constant γ , when it is weighted by a factor depending on the mean depth of the cell $\rho_j \left(\frac{1}{\langle z_j + \epsilon \rangle} \right)$, where ϵ is a small number to avoid singularity at the surface). This artifice is used by some authors (Li and Oldenburg 1996; Pilkington 1997) to give an equi-probability to each cell during the inversion process and to desensitize cells at the surface. Figure 2(b) shows a cross-section of the contributions of each cell to the gravity observation at the surface. Obviously the sensitivity is highest on near-surface cells. Thus every density distribution will be preferably determined at the surface if the matrix G is not altered. Figures 2 and 3 show how the kernel calculated using (2) reacts when weighted by $\frac{1}{\langle z_j + \epsilon \rangle^\beta}$ with three distinct values of β . For $\beta = 0.0$, the form is 'natural' and pictured as a shallow hemisphere. In the case of $\beta = 0.8$, the pattern is spread like a bulb (Fig. 3a) giving more emphasis to intermediate depths. For $\beta = 1.9$, the sensitivity is practically constant just under the station g_i at coordinate $(0, 0, -0.1)$. A consequence would be to yield extreme density contrast and concentrate the solution at depth. On these figures, we see that the maximum sensitivity with depth lies approximately on the straight line $z = \left[\frac{1+\beta}{2-\beta} \right]^{\frac{1}{2}} x$, calculated with a simple spherical model. Proof is given in the next section. Numerous tests on synthetic inversion indicate that a weight depending on a power β , such as $\frac{1}{\langle z_j + \epsilon \rangle^\beta}$, is appropriate for adjusting the

reconstruction of synthetic bodies. The best value found in our tests is $\beta = 0.9$ and an acceptable range is $[0.5, 1.0]$. Li and Oldenburg (1998) used a weighting function which takes account of the elevation z_0 of the gravity station ($w(z) = \langle z + z_0 \rangle^{-\beta/2}$). In our case, data are always inverted at elevation $z_0 \ll \delta z$ and results are not affected by our depth weighting function. Inclusion of the elevation z_0 in the weighting function is made if needed.

Model domain for inversion

A method is proposed for choosing automatically the dimensions of the inversion domain in the x - and y -directions by padding (*pad*) the gravity data grid with cells around it, therefore avoiding possible distortion in the reconstruction along the boundary. To obtain an analytical formulation, the subsurface is modelled by a network of spheres of radius r_s . The associated analytical kernel G_s is given by

$$G_s = \gamma \frac{4}{3} \pi r_s^3 \frac{(z + \epsilon)}{(x^2 + y^2 + (z + \epsilon)^2)^{\frac{3}{2}}} \quad (4)$$

We want to know the influence of a cell B on a reference cell A located at the surface (see Fig. 1). As the inversion reconstruction favours the cells at the surface, a weight Q is introduced, which depends on the inverse mean depth for each cell, such as

$$Q = \frac{1}{\langle z + \epsilon \rangle^\beta} \quad (5)$$

The sensitivity kernel G_s is weighted with the scalar Q giving a new kernel denoted by $G_{s,\beta} = G_s Q^{-1}$. The maximum of the function $G_{s,\beta}$ with respect to z ($\frac{\partial G_{s,\beta}}{\partial z} = 0$) leads to

$$(z + \epsilon) = \left(\frac{1 + \beta}{2 - \beta} \right)^{\frac{1}{2}} d, \quad (6)$$

where $d = [x^2 + y^2]^{\frac{1}{2}}$ is the polar distance in the $(x-y)$ -plane. Along this straight line (equation (6)), we have the maximum of sensitivity with depth $G_{s,\beta}$ (for $\beta = 0$, without weighting, the relationship is $z = 0.7 * x$ in the $(x-z)$ -plane). If we replace (6) in the function $G_{s,\beta}$, we obtain $G_{s,\beta}^{\text{MAX}}$, given by

$$G_{s,\beta}^{\text{MAX}} = \gamma \frac{4}{3} \pi r_s^3 \frac{(1 + \beta)^{\frac{1+\beta}{2}} (2 - \beta)^{\frac{2-\beta}{2}}}{3\sqrt{3} d^{2-\beta}} \quad (7)$$

Now we compare the influence of the sensitivity $G_{s,\beta}^B$ of a cell B (Fig. 1) to the sensitivity $G_{s,\beta}^A$ of a reference cell A located at the surface along the line defined by (6). In this way we define an admissible threshold q chosen so that $\frac{G_{s,\beta}^B}{G_{s,\beta}^A} \leq q \%$,

with $G_{s,\beta}^A = \gamma \frac{4}{3} \pi r_s^3 (r_s)^{\beta-2}$ at $(x_j, y_j, z_j) = (0, 0, r_s)$ and $G_{s,\beta}^B = G_{s,\beta}^{\text{MAX}}$. We find an inequality for the polar distance d , given by

$$d \geq \frac{(1 + \beta)^{\frac{1+\beta}{4-2\beta}} (2 - \beta)^{\frac{1}{2}}}{\left(3\sqrt{3} * \frac{q}{100}\right)^{\frac{1}{2-\beta}}} r_s. \quad (8)$$

In practice, we replace r_s by the increment of the prism in the z -direction ($\delta z = 2r_s$) and divide the length d by the minimum between the two increments δx and δy . Thus the number of extra cells to add around the domain is $pad = \frac{d}{\min\{\delta x, \delta y\}}$. As a result, the minimum storage for the sensitivity matrix is equal to $(nox + pad) * (noy + pad) * nc_z$, where nox and noy are the number of observations in the x - and y -directions, and nc_z is the number of cells in the z -direction.

Cell size

The determination of the optimum cell size for a given problem is fundamental in inversion. Two competing criteria have to be considered: (i) a sufficiently small cell size such that short wavelengths present in the observed data can be modelled; (ii) a sufficiently large cell size such that the total number of parameters to invert for remains limited and allows computation to take place within a reasonable time. In Appendix A, we develop the necessary formulation to address the problem. We conclude that the maximum cell size which is able to fit the shortest wavelength in the data should be less than $1.2\delta x$, where δx is the distance between gravity observations. In the inversion code discussed here, we always take a cell size equal to δx . This is a general rule, also used by other authors (Li and Oldenburg 1996).

FORMULATION

The formulation of an inverse problem consists of finding an acceptable model closest to an initial guess (Backus and Gilbert 1967). The inversion using the criterion of minimum distance as proposed by Green (1975) consists of minimizing the distance of an acceptable model from an initial one, subject to an equality constraint ($\mathbf{g}^{\text{obs}} - \mathbf{g} = \mathbf{G}(\boldsymbol{\rho} - \boldsymbol{\rho}^0)$) imposed through the Lagrange multipliers. We rewrite here the Lagrangian function $L(\boldsymbol{\rho}, \boldsymbol{\theta})$ which minimizes the semi-norm $\frac{1}{2} \|\mathbf{W}(\boldsymbol{\rho} - \boldsymbol{\rho}^0)\|_2^2$, subject to equality constraints $\mathbf{A}(\boldsymbol{\rho} - \boldsymbol{\rho}^0) = \mathbf{b}$, in a standard form (Gauvin 1995) as

$$L(\boldsymbol{\rho}, \boldsymbol{\theta}) = \frac{1}{2} (\boldsymbol{\rho} - \boldsymbol{\rho}^0)^T \mathbf{W}^T \mathbf{W} (\boldsymbol{\rho} - \boldsymbol{\rho}^0) + (\mathbf{b} - \mathbf{A}(\boldsymbol{\rho} - \boldsymbol{\rho}^0))^T \boldsymbol{\theta}. \quad (9)$$

The Lagrangian function $L(\boldsymbol{\rho}, \boldsymbol{\theta})$ is composed of augmented matrices (Jackson 1979; Pilkington 1997):

- $\mathbf{A}^T = [\mathbf{G}^T | \mathbf{H}^T]$, where $\mathbf{G}_{N \times M}$ is the sensitivity matrix and $\mathbf{H}_{M \times M}$ is the first centred derivative ($\xi_H \partial$) or the second derivative ($\xi_H \partial^2$) matrix. ξ_H is a coefficient giving either more or less importance to the matrix \mathbf{H} . The first and the second derivatives are usually referred to as ‘flatness’ and ‘smoothness’ constraints in the literature. In practice we choose ξ_H as the square norm of the matrix $\|\mathbf{G}\mathbf{x}\|^2$ with $\|\mathbf{x}\| = 1$ (Golub and van Loan 1996) multiplied by a small number μ_H ($\xi_H = \mu_H \|\mathbf{G}\mathbf{x}\|^2$). In the tests presented in this paper $\mu_H = 10^{-4}$ was used. If the balancing coefficient ξ_H is too large when the conjugate gradient is running, we choose to decrease ξ_H iteratively by a factor to ensure convergence.
- $\mathbf{b}^T = [\Delta \mathbf{g}^T | \mathbf{0}^T]$, where the vector $\mathbf{b}_{1 \times (N+M)}$ consists of $\Delta \mathbf{g}$ which is the difference between the observed \mathbf{g}^{obs} and the calculated \mathbf{g} anomaly, and a null vector $\mathbf{0}$.
- $\boldsymbol{\theta}^T = [\boldsymbol{\alpha}^T | \boldsymbol{\zeta}^T]$, where $\boldsymbol{\theta}_{1 \times (N+M)}$ is a Lagrange multiplier associated with equality constraints and is split into two others ($\boldsymbol{\alpha}$ for $\Delta \mathbf{g}$ and $\boldsymbol{\zeta}$ for $\mathbf{0}$).
- $\boldsymbol{\rho}^0$ is the vector of initial contrasts of density.
- $\mathbf{W}_{M \times M} = \mathbf{P}^{-1} \mathbf{Q} \mathbf{V}$ is equal to the product of three diagonal matrices \mathbf{P} , \mathbf{Q} and \mathbf{V} .
- \mathbf{P} is the matrix of the ‘hard’ constraint, where P_{jj} is fixed at $\eta \approx 10^{-2}$ or 1 depending on whether the value of the j th initial contrast of density ρ_j^0 is fixed by geological information or not, respectively. Moreover, if ρ_j takes a value beyond the global limits defined by $\rho_{\min} \leq \rho_j \leq \rho_{\max}$, P_{jj} is fixed at η .
- \mathbf{Q} is the depth weighting matrix with diagonal elements $Q_{jj} = \frac{1}{(z_j + \epsilon)^\beta}$.
- The matrix \mathbf{V} is a minimum volume constraint where $V_{jj} = \frac{\max\{|\rho_j|\}}{\alpha_V(|\rho_j| + 10^{-3})}$. α_V is a coefficient giving more or less importance to the minimum volume constraint. For $\alpha_V = 1$, V_{jj} take values between 0 and 1. The scalar $\max\{|\rho_j|\}$ avoid huge increases in V_{jj} and numerical instability. When all ρ_j are equal to zero, we assign $V_{jj} = 1$. The effect of this constraint is to concentrate the solution in a minimum volume by decreasing the amplitude of small contrast of density ρ_j . The constraint of Last and Kubik (1983), which minimizes the volume or maximizes the compactness, is formulated as $V_{jj} = \frac{1}{\rho_j^2 + \epsilon}$ and differs from V_{jj} . However, the global aim of V_{jj} and \tilde{V}_{jj} is the same. $\mathbf{V} \equiv \mathbf{I}$ if we do not use the minimum volume constraint.

Minimization of the objective function $L(\boldsymbol{\rho}, \boldsymbol{\theta})$ with respect to the contrast of density $\boldsymbol{\rho}$ and the Lagrange multipliers $\boldsymbol{\theta}$ vectors gives, after some manipulations, a system of two

equations. This system is solved iteratively and can be written as

$$(\mathbf{A}\mathbf{W}^{-1})(\mathbf{A}\mathbf{W}^{-1})^T \boldsymbol{\theta}^k = \mathbf{b}^k, \quad (10)$$

$$\boldsymbol{\rho}^{k+1} = \boldsymbol{\rho}^k + \mathbf{W}^{-1}(\mathbf{A}\mathbf{W}^{-1})^T \boldsymbol{\theta}^k. \quad (11)$$

\mathbf{W} is modified at each iteration k . At each iteration k , we find a solution $\boldsymbol{\theta}^k$ of (10) with an rms_{CG}^k error $\leq 10^{-1} * rms_{CG}^0$ (CG denotes conjugate gradient). $\boldsymbol{\theta}^k$ is replaced in (11) to give the solution $\boldsymbol{\rho}^{k+1}$. The anomaly \mathbf{g}^{k+1} and the vector $\Delta \mathbf{g}^{k+1}$ are calculated to estimate a global rms_{GL} error or a χ^2 magnitude ($\chi^2 = \|\frac{g_i^{obs} - g_i}{\sigma_i}\|_2^2$ where σ_i is the error standard deviation). The program stops when it reaches the rms_{GL}^k error target $\leq 10^{-2} * rms_{GL}^0$ or $\chi^2 \leq N + \sqrt{2N}$, and/or a maximum of iterations. Successive solutions can be viewed as an increment $\Delta \boldsymbol{\rho}^k$ added to the current contrast of density $\boldsymbol{\rho}^k$ yielding $\boldsymbol{\rho}^{k+1} = \boldsymbol{\rho}^k + \Delta \boldsymbol{\rho}^k$. $\Delta \boldsymbol{\rho}^k$ can be expressed as

$$\Delta \boldsymbol{\rho}^k = \mathbf{W}^{-1}(\mathbf{A}\mathbf{W}^{-1})^T ((\mathbf{A}\mathbf{W}^{-1})(\mathbf{A}\mathbf{W}^{-1})^T)^{-1} \mathbf{b}^k. \quad (12)$$

The code works with absolute values of density in the input file, and a background density value ρ_B is assigned by the user. ρ_B is subtracted from the density of all prisms to obtain density contrasts. The code is stable with respect to background density variations since density contrasts are added at each iteration around $\boldsymbol{\rho}^0$.

Equation (10) can be written explicitly as

$$\begin{bmatrix} \mathbf{G}\mathbf{W}^{-1} \\ \mathbf{H}\mathbf{W}^{-1} \end{bmatrix} \begin{bmatrix} \mathbf{W}^{-1}\mathbf{G}^T & \mathbf{W}^{-1}\mathbf{H}^T \end{bmatrix} \begin{bmatrix} \boldsymbol{\alpha} \\ \boldsymbol{\zeta} \end{bmatrix} = \begin{bmatrix} \Delta \mathbf{g} \\ 0 \end{bmatrix}. \quad (13)$$

The first implementation of the problem did not make use of the flatness/smoothness constraint ($\mathbf{A} \equiv \mathbf{G}$). It was solved using the singular value decomposition of the product $(\mathbf{G}\mathbf{W}^{-1})(\mathbf{G}\mathbf{W}^{-1})^T = \mathbf{V}\mathbf{L}\mathbf{V}^T$, where \mathbf{L} and \mathbf{V} correspond to the eigenvalue and eigenvector matrices, respectively. The system to resolve is $\mathbf{V}\mathbf{L}\mathbf{V}^T \boldsymbol{\alpha} = \Delta \mathbf{g}$ and the solution of the estimated Lagrange multiplier $\boldsymbol{\alpha}$ is given by Lines and Treitel (1984) as

$$\boldsymbol{\alpha} = \mathbf{V}\mathbf{L}(\mathbf{L}^2 + \lambda\mathbf{I})^{-1}\mathbf{V}^T \Delta \mathbf{g}, \quad (14)$$

where λ is the Marquardt damping factor. However, this solution is not tractable when the number of data is large. Therefore we use the conjugate-gradient method (Golub and Van Loan 1996) to resolve the system of equations (13). A special case was made to solve (14) using the conjugate gradient when $\mathbf{A} \equiv \mathbf{G}$. In fact the product $\mathbf{U} = (\mathbf{G}\mathbf{W}^{-1})(\mathbf{G}\mathbf{W}^{-1})^T$ is a square positive-definite matrix and if we scale it

with its diagonal ($\mathbf{U}_d = \text{diag}(\mathbf{U})$), we obtain the scaled system,

$$\mathbf{U}_s \boldsymbol{\alpha}_s = \Delta \mathbf{g}_s, \quad (15)$$

where $\mathbf{U}_s = \mathbf{U}_d^{-1/2} \mathbf{U} \mathbf{U}_d^{-1/2}$, $\boldsymbol{\alpha}_s = \mathbf{U}_d^{-1/2} \boldsymbol{\alpha}$, and $\Delta \mathbf{g}_s = \mathbf{U}_d^{-1/2} \Delta \mathbf{g}$. Thus the distinctive property of the matrix \mathbf{U}_s is its symmetry which enables us to obtain all its elements using only the first row of \mathbf{U}_s . The amount of memory to store becomes a vector of length $(1 \times N)$ instead of an $(N \times N)$ matrix. Furthermore, updating and resolution of the system become very fast.

THE MULTIGRID TECHNIQUE

The multigrid technique is generally used to resolve discretized differential equations with iterative or relaxation methods. A good tutorial has been given by Briggs (1987) and a more detailed analysis by Hackbusch and Trottenberg (1982). The aim of our approach is to use this technique for the under-determined inverse problem. Thus we decided to sample gravity observations in the x - and y -directions to solve first for long anomaly wavelengths and then for short wavelengths. This is necessary in order to decompose the observation set into several levels. The first level is the finest, composed of all data, and the last one is the coarsest. In the case of two levels, we solve the system of equations (10) and (11) with $\mathbf{A} \equiv \mathbf{G}$ for the coarse level. The density found for this level is transferred by a trilinear interpolation to the finest level. The same equations are now solved for the finest level giving the final density result. The same global rms_{GL} error or χ^2 magnitude is used for each level. If the number of levels is greater than two, we run these levels in a different manner by designing a cycle. More details of how we use the multigrid method are given in Appendix B.

MODELLED DATA

Dipping dike

For testing the program, we use a simple dipping dike model of density 0.2 g/cm^3 placed in a background of $\rho_B = 0 \text{ g/cm}^3$ (see Fig. 4). This synthetic model is geometrically the same as that used by Li and Oldenburg (1996, 1998). Figure 5 shows the anomaly calculated from this synthetic model. The subsurface is divided into $21 \times 21 \times 10 = 4410$ cubic cells of 1 km edge. Gravity effects g_i are computed at the surface directly above the centre of the cells at $z_i = -0.1 \text{ m}$. The data have been contaminated by uncorrelated Gaussian noise of maximum amplitude 0.5 mGal . We generate the noise vector \mathbf{v}_n added to \mathbf{g}^{obs} as $\mathbf{v}_n = [0.5\% \text{ var}(\mathbf{g}^{obs})]^{1/2} * N(0, 1) \approx 0.12 * N(0, 1)$,

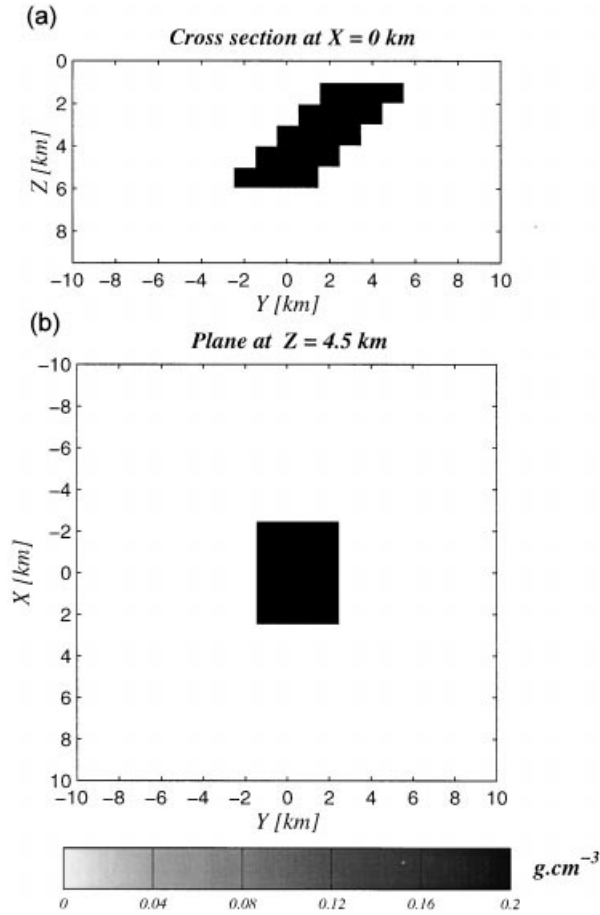


Figure 4 Model of a dipping dike set in a grid of $21 \times 21 \times 10$ cells of side 1 km. (a) Cross-section at $X = 0$ km; (b) plane at $Z = 4.5$ km. The density contrast of the dike is 0.2 g/cm^3 .

where $N(0,1)$ denotes normally distributed random numbers with maximum amplitude of ± 5 . $\text{var}(g^{\text{obs}})$ is the variance of the observed data g^{obs} . In each figure, a cross-section at $x = 0$ km and a plane at $z = 4.5$ km are shown. The starting model for inversion is a homogeneous ground with density $\rho^0 = 0$ and the initial penalty matrix $\mathbf{P} = \mathbf{I}$. Positivity of ρ^k is imposed here during the inversions on synthetic data by cutting out densities beyond the global limits $[\rho_{\min}, \rho_{\max}]$, chosen to be 0 and 0.2 g/cm^3 , respectively, otherwise small negative amplitudes of ρ^k are observed around the dike. For all inversion tests, the coefficient β in the weighting criterion Q is fixed at 0.9 and $\alpha_V = 1$ to compare all techniques. The program stops when $\chi^2 \leq 470$. $\sigma_i = 0.5 \text{ mGal}$ for all stations.

Figure 6 shows the results of inversion using only the minimum distance constraint (Green 1975) for recovering the

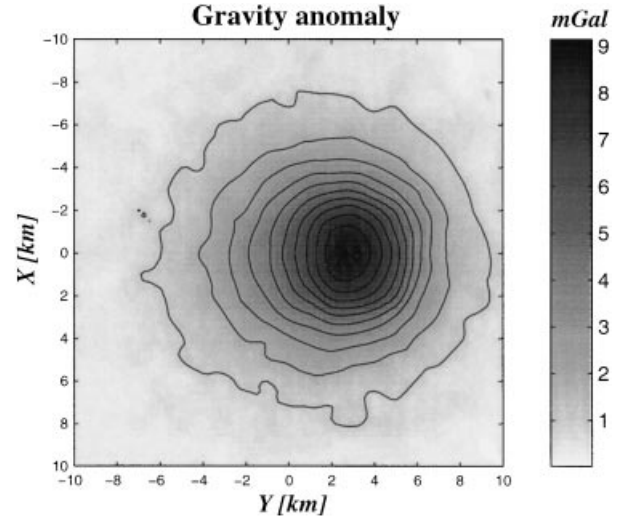


Figure 5 Anomaly due to the synthetic model shown in Fig. 4 and contaminated by uncorrelated Gaussian noise.

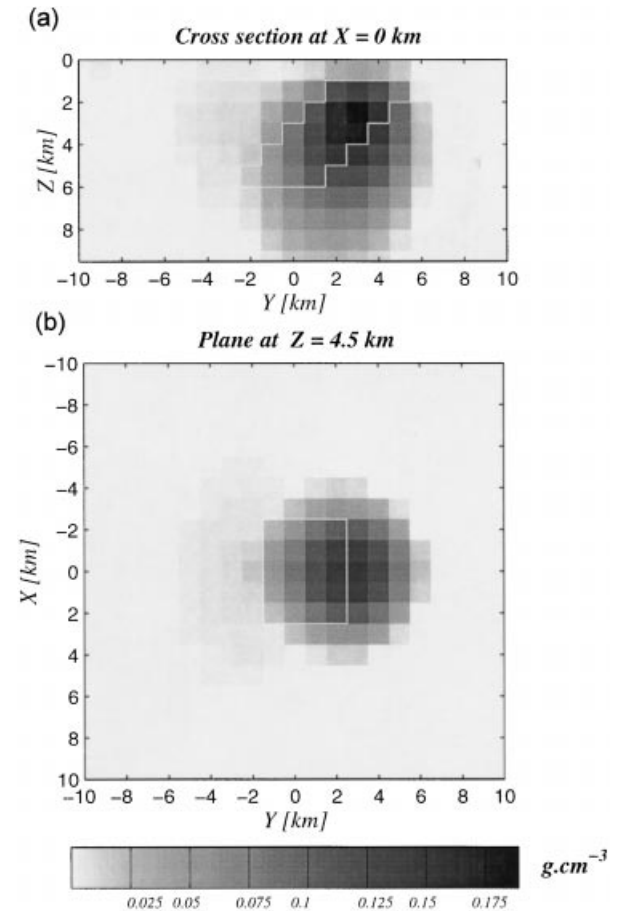


Figure 6 Density model obtained from inverting data of Fig. 5 using only the minimum distance formulation. $\beta = 0.9$ and a global misfit $\chi^2 = 470$ are used.

density model. We find a density value of 0.185 g/cm^3 and a good estimate of the depth to the top of the dike, but its slope cannot be recovered (the white line contours the initial dike model in Figs 6–10). This behaviour is due to the sensitivity pattern shown in Fig. 3 which spreads the solution as the depth increases. For compact bodies without anisotropy, this type of inversion gives good results with a good spatial resolution only in the x - and y -directions. Tests have been made for different values of the coefficient β in the range $[0.5, 1]$ and the effect is to move the solution slightly in the vertical direction. Figure 7 shows the resulting model for the multigrid technique with an FMV cycle with a maximum level equal to 3. The reconstruction shows a compact image with a maximum density value of 0.185 g/cm^3 . The solution is not perfect, but it is attractive because it is quickly obtained by taking advantage of the matrix symmetry explained in

(15). This technique is not really appropriate for a synthetic model with only one body, but it could be an interesting technique in the case of multiple bodies for which combinations of long and short wavelengths are expected. Moreover, experience shows that the coefficient β must be chosen to be 0.8 to best replace the top of bodies. Tests were made using the multigrid technique and the flatness constraint jointly, but improvement was not found to be significant. A reconstruction can be made using only the flatness operator, giving a good estimate of the density 0.185 g/cm^3 (see Fig. 8). The two last inversions use the criterion of minimum volume in conjunction with depth weighting. Figure 9 leads to a better solution with a maximum density of 0.2 g/cm^3 . The limits of the dike are better restricted by eliminating the ‘natural’ diffuse behaviour visible in the preceding figures. By using the minimum volume criterion and the flatness operator, the

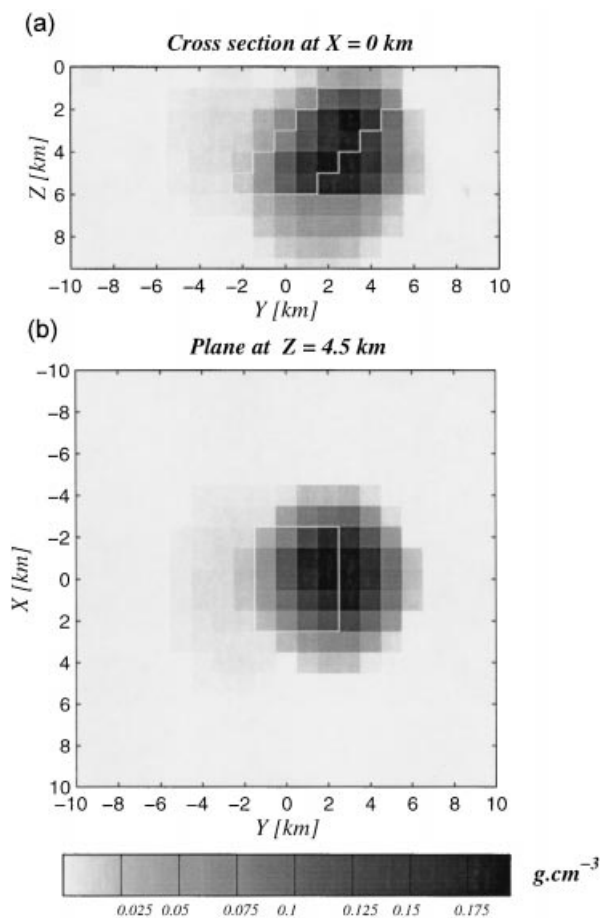


Figure 7 Density model obtained from inverting data of Fig. 5 using only the multigrid technique (FMV cycle with a maximum level of 3). $\beta = 0.9$ and a global misfit $\chi^2 = 470$ are used.

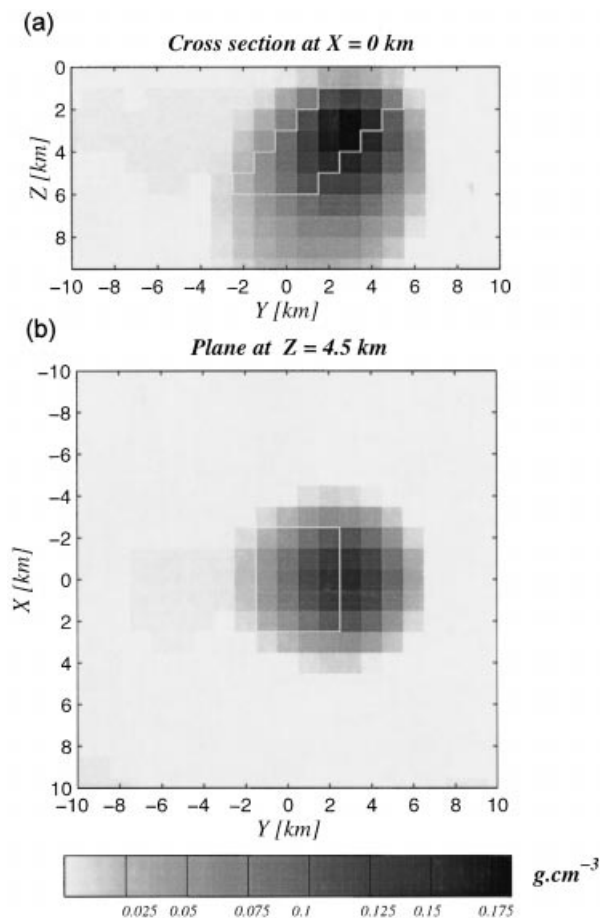


Figure 8 Density model obtained from inverting data of Fig. 5 using only the flatness constraint without the minimum volume constraint. $\beta = 0.9$ and a global misfit $\chi^2 = 470$ are used.

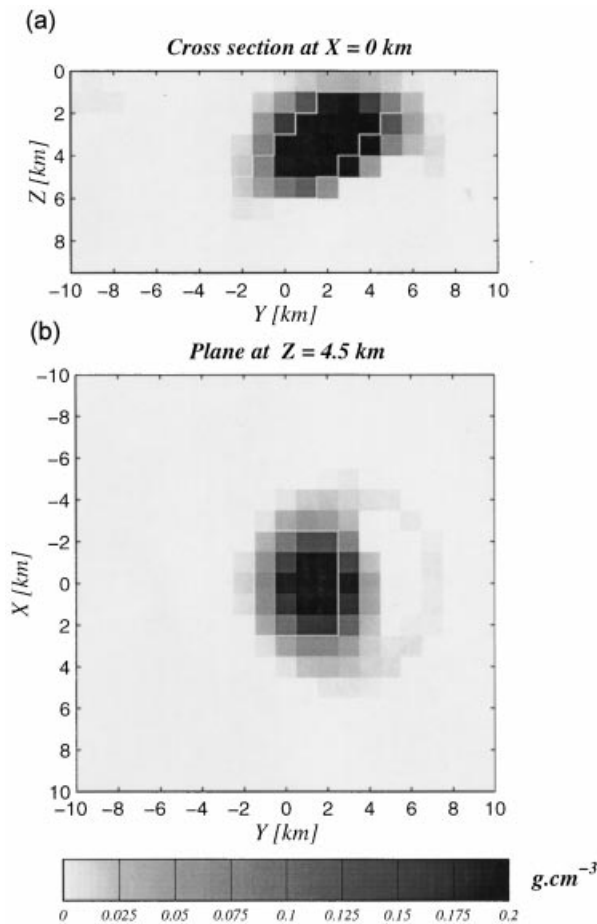


Figure 9 Density model obtained from inverting data of Fig. 5 using only the minimum volume constraint. $\beta = 0.9$ and a global misfit $\chi^2 = 470$ are used.

solution of the last test (Fig. 10) gives a good density estimate of 0.2 g/cm^3 . The last two inversions seem to best recover the geometry and density value for the dike model.

Multiple bodies

With this modelled data, we want to explore the ability and limitation of the current formulation to recover more complex structures from gravity data, i.e. contiguous bodies with various depths, sizes and geometries. Figure 11 shows a plan view and a vertical section of the modelled structures consisting of blocks lighter (-0.2 g/cm^3) and denser ($+0.18 \text{ g/cm}^3$) than the background (2.82 g/cm^3). Figure 12 shows the gravity anomaly contaminated by uncorrelated Gaussian noise of maximum amplitude 0.5 mGal and computed from the model at the surface (29×36 stations

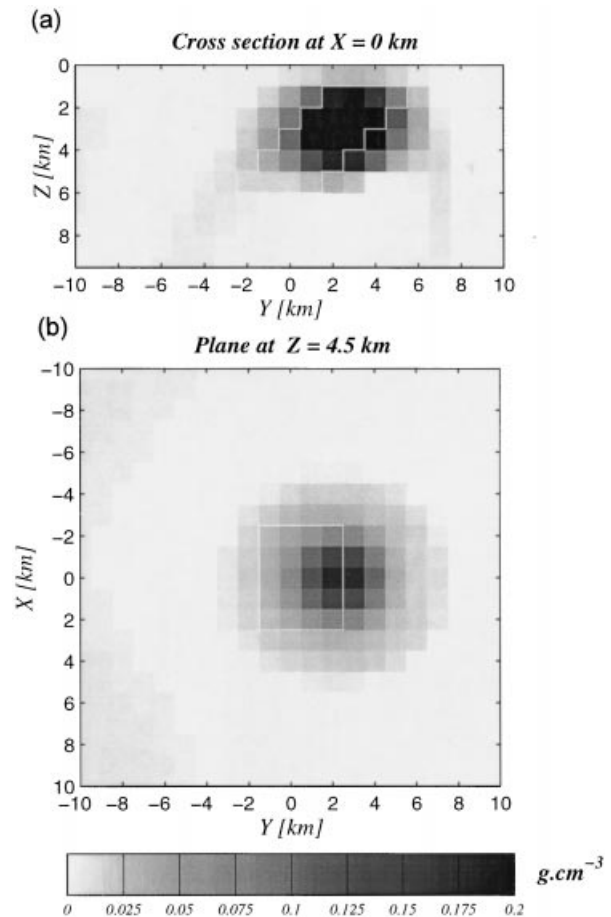


Figure 10 Density model obtained from inverting data of Fig. 5 using flatness and minimum volume constraints. $\beta = 0.9$ and a global misfit $\chi^2 = 470$ are used.

and $35 \times 42 \times 10$ parameters). Inversion was performed using alternative constraints, as on the previous dike model. Figure 13 shows the resulting model for inversion using compactness ($\alpha_v = 1$) and flatness constraints with $\beta = 0.9$. Convergence was reached after three iterations. CPU time on a Sparc Ultra-1 143 MHz SUN workstation was 35 minutes. The horizontal position of all the bodies is well recovered in the two results. Depths to the top are also generally close to those of the model. Only extensions of the largest bodies appear to be overestimated in Fig. 13. This could be caused by the lack of sensitivity of the response to the deeper part of the model. In addition, the data set shown in Fig. 12 is a limited window over the complete anomaly; truncation of the anomalies may play a role in blurring the reconstructed model. However, this test on multiple bodies enables us to estimate the resolving power of the inversion method in real applications where the geology is more complex than the dike

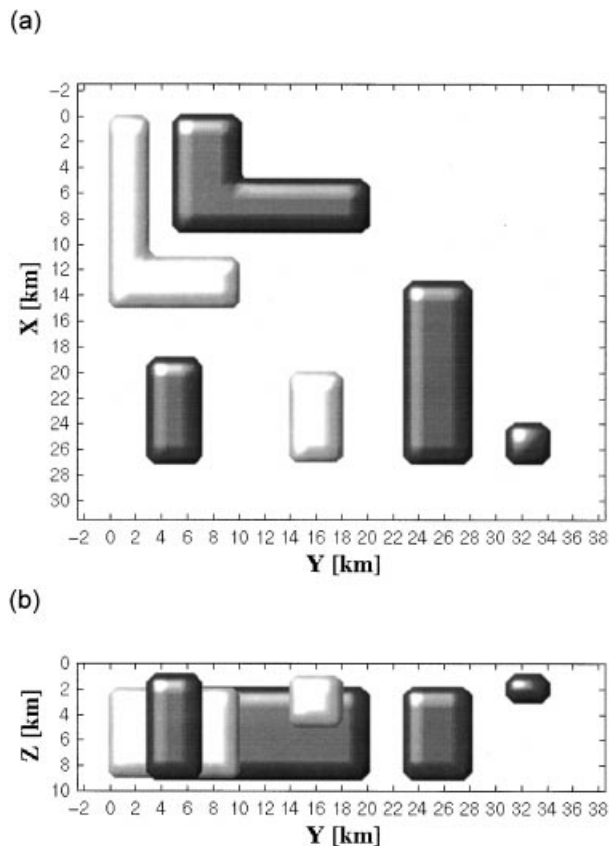


Figure 11 Model of multiple bodies. (a) Plan view; (b) vertical section. Lighter and denser blocks have density contrasts of -0.2 g/cm^3 (pale grey) and $+0.18 \text{ g/cm}^3$ (dark grey) compared with the background density of 2.82 g/cm^3 .

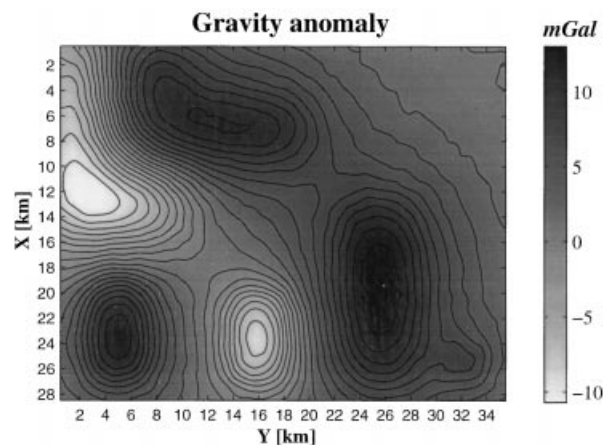


Figure 12 Anomaly due to the synthetic model shown in Fig. 11 and contaminated by uncorrelated Gaussian noise.

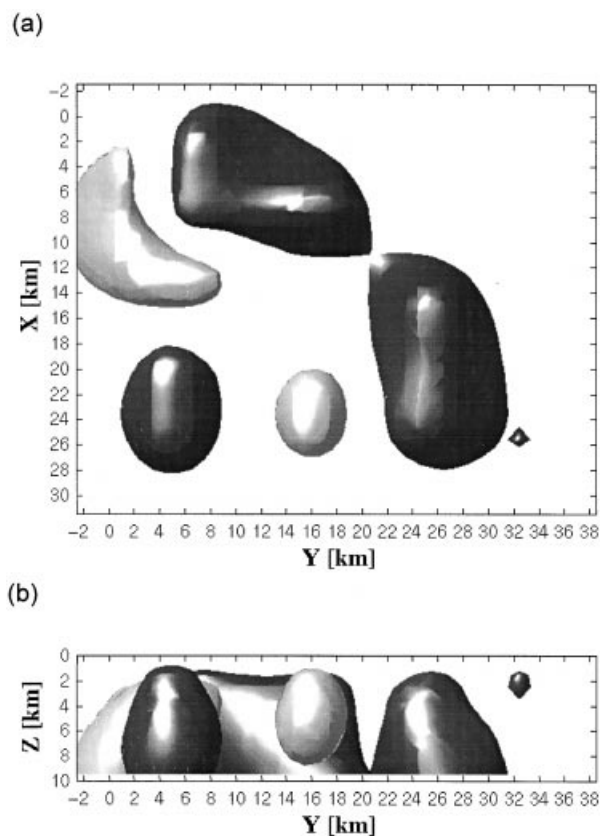


Figure 13 Density model obtained from inverting data of Fig. 12 using flatness and minimum volume constraints. $\beta = 0.9$ and a global misfit $\chi^2 = 1089$ are used.

model. This is particularly true for the next application in Abitibi.

TEST ON REAL DATA

Geological context

The data used for testing the inversion code cover the Blake River Group, a subdivision of the Abitibi Greenstone Belt in Quebec (Canada), well known for the Cu–Zn–Au rich mining camp of Rouyn-Noranda. The Blake River Group is located between the Destor-Porcupine Fault (DPF) to the north and the Larder Lake-Cadillac Fault (LLCF) to the south (Fig. 14). Inside the andesite-basalt matrix (2.85 g/cm^3) composed of several volcanic cycles (Gibson and Watkinson 1990; Pélouin *et al.* 1990), the region is intruded by syn- or post-volcanic granodiorite-tonalite (2.74 g/cm^3) plutons mapped at the surface, such as the Flavrian pluton (FP) and the Dufault pluton (DP). Rhyolitic rocks (2.7 g/cm^3) alternate with andesitic flows in the volcanic sequence and are mainly

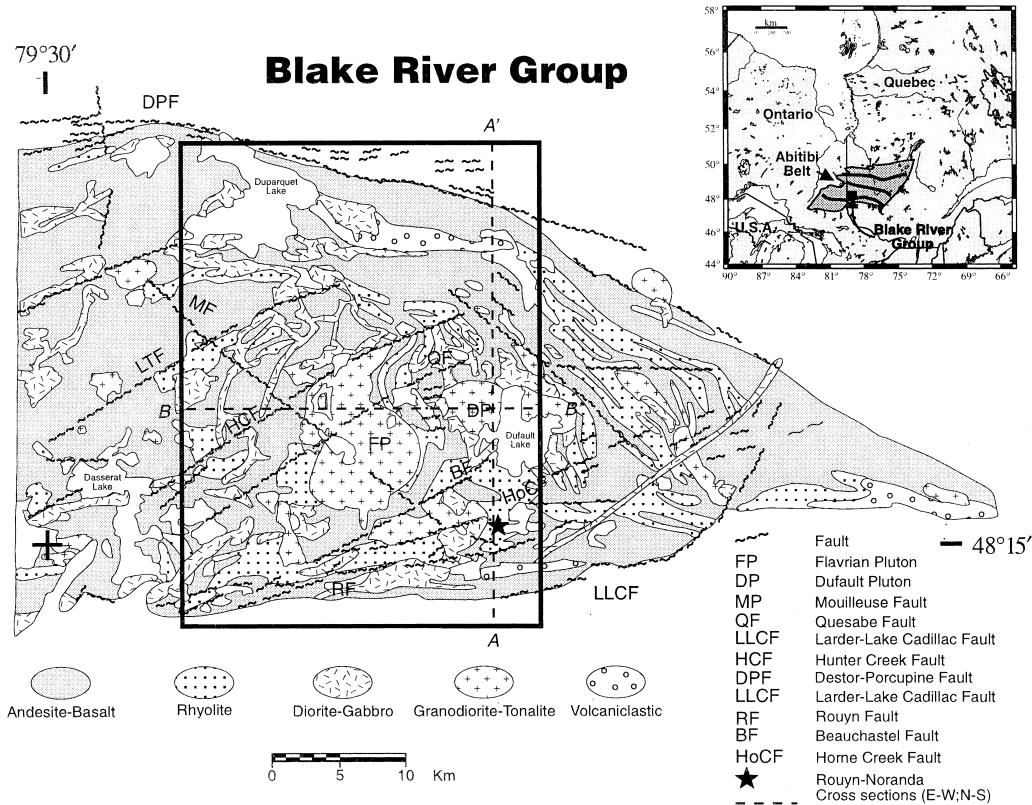


Figure 14 Geological map of the northern part of the Rouyn-Noranda mining camp. Major lithological contacts and faults are shown. The black box indicates the area mapped by gravity data. Black dotted lines indicate cross-sections chosen among the results of reconstruction shown in Fig. 16 with the observed data set mapped in Fig. 15.

mapped along the Larder Lake-Cadillac Fault over about 30 km in the W–E direction and in the eastern part of the Dufault pluton in the NW–SE direction. It is generally at the contact between felsic-rhyolites and mafic andesites that massive sulphide mineralization is found. Some diorite-gabbro ($>3 \text{ g/cm}^3$) dikes and sills cut the Blake River Group in a SW–NE direction, more or less parallel to the Hunter Creek and Lake Tarssac faults (HCF and LTF). The volcanoclastic rocks (2.85 g/cm^3) are more scattered and are found along the DPF and LLCF faults. The gravity data used here are extracted from a larger data set. The test zone ($28 \times 35 \text{ km}^2$ area) is delimited by a black box in Fig. 14. Black dotted lines indicate cross-sections chosen from the results of inversion shown in Figs 16 and 17.

Residual Bouguer anomaly

The gravity data collected in the north-west area of Rouyn-Noranda between UTM coordinates [622000, 650000] East and [5340000, 5375000] North have been corrected for topography. They consist of 1056 stations. The Bouguer

anomaly corresponding to a 1 km square grid is obtained by kriging gravity data with a Gaussian model. The residual Bouguer anomaly (Fig. 15) is obtained by subtracting the regional anomaly obtained by upward continuation of the Bouguer anomaly at 20 km (Jacobsen 1987) from the Bouguer anomaly. It reaches a maximum magnitude of about 17 mGal. The residual anomaly displays extreme magnitudes in four major areas. The west section has the greatest amplitude associated with andesite-basalt rocks and a SW–NE strike. The central-south section has the lowest amplitude and coincides with the Powell at [East, North] = [640, 5345] km. In the north section, an elongated anomaly between -0.87 and 2.94 mGal corresponds to a gabbro-diorite unit appearing on the surface. Another weak magnitude anomaly is located in the central-east section and corresponds to the Dufault pluton ([East, North] = [647, 5355] km). The Flavrian pluton observable on the geological map is located at the centre. Faults and plutons are positioned schematically to better correlate positive and negative amplitudes of the residual anomaly with the known geology. The road and the city of Rouyn are exactly located.

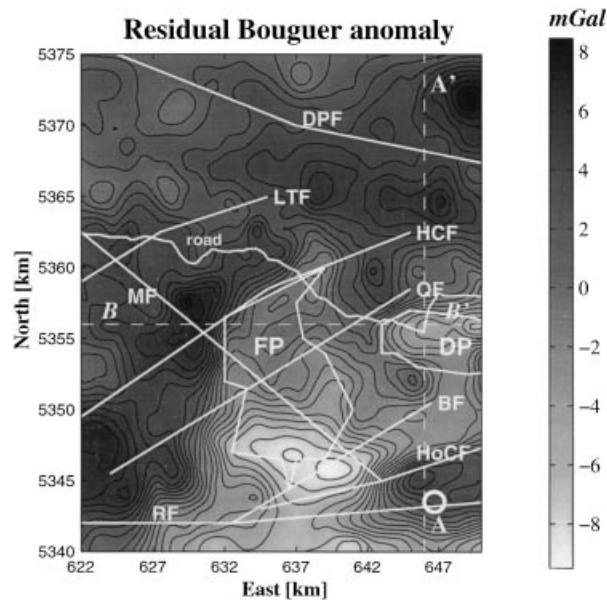


Figure 15 Residual Bouguer anomaly over the Blake River Group (Abitibi region, Quebec). White dotted lines indicate cross-sections shown in Fig. 16. The circle is city of Rouyn-Noranda. See Fig. 14 for abbreviations of geological structures.

Inversion result

The residual Bouguer anomaly (Fig. 15) was sampled every 1 km for the inversion (29×36 gravity stations). The subsurface is discretized into cells of side 1 km; the domain is enlarged in the x - and y -directions with three cell-wide walls corresponding to $q = 5\%$, defined in (8), resulting in a model subsurface parametrization of $35 \times 42 \times 10$ prisms. Inversion is carried out with *a priori* information about the background density ρ_B of 2.82 g/cm^3 (see Bellefleur 1992). A combination of flatness and minimum volume constraints are appropriate for mineral exploration when trying to detect dipping bodies with a high density contrast. A weight Q with $\beta = 1$ and an rms_{GL}^k error $\leq 10^{-2} * \text{rms}_{\text{GL}}^0$ and rms_{CG}^k error $\leq 10^{-1} * \text{rms}_{\text{CG}}^0$ are used. The time to execute this is about 3 hours and the amount of memory required is 3.5 MB in double precision on an Ultra-1 143 MHz SUN workstation. Figures 16 and 17 show the result of the 3D inversion of the Blake River Group. Two cross-sections located at East = 646 km and North = 5356 km are visible in Fig. 16. We observe on cross-section A–A' the mafic volcanic complex of Rouyn (C×R) with a density greater than 2.85 g/cm^3 and the Dufault Pluton (DP) with a density smaller than 2.74 g/cm^3 (see Perron and Calvert 1998 for the choice of density values). The C×R has a vertical extension of about 8 km, whereas the DP seems to stop at 5 km. Bellefleur (1992) and

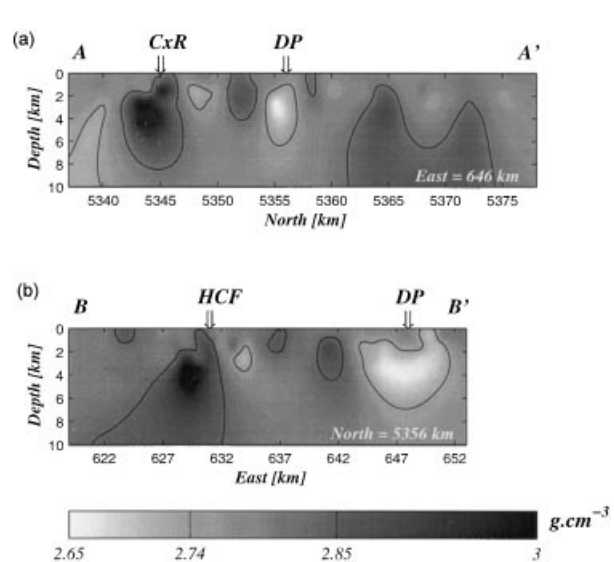


Figure 16 Results of 3D inversion of the Blake River Group data using $\beta = 1.0$, flatness operator and minimum volume constraint ($\alpha_V = 0.1$). (a) North-South cross-section A–A' at position East = 646 km. (b) West-East cross-section B–B' at position North = 5356 km. DP, Dufault Pluton; C×R, volcanic Complex of Rouyn; HCF, Hunter Creek Fault.

Deschamp, Chouteau and Dion (1993) estimated the same vertical extension of 6 km for the C×R. Keating (1992, 1993) found a vertical extension of more than 6 km and mentioned that the effect of a 2D inversion compared with a 3D inversion is to underestimate thicknesses. The shapes of these two major bodies show a trend in the E–W direction, visible in Fig. 17. The 3D inversion result is in agreement with the major lithological contacts and gives more exact information about the volume of plutons and intrusive rocks. Major structures and faults are drawn with black lines in Fig. 17. Correlation can be made with the Lithoprobe seismic reflection profiles 14 and the 3D density distribution to identify the DPF fault visible in Fig. 17 (see Green *et al.* 1990). High-resolution and regional seismic reflection have been carried out along the Lithoprobe line 21 which is coincident with the road in Fig. 17. Verpaelt *et al.* (1995) found a 'northeast-facing dip to the Blake River Group central mines sequence, which has been disrupted by the sub-vertical Hunter Creek fault'. Hunter Creek fault is located on the cross-section B–B' in Fig. 16(b) at position East = 630 km.

DISCUSSION AND CONCLUSIONS

The 3D gravity inversion using the criterion of minimum

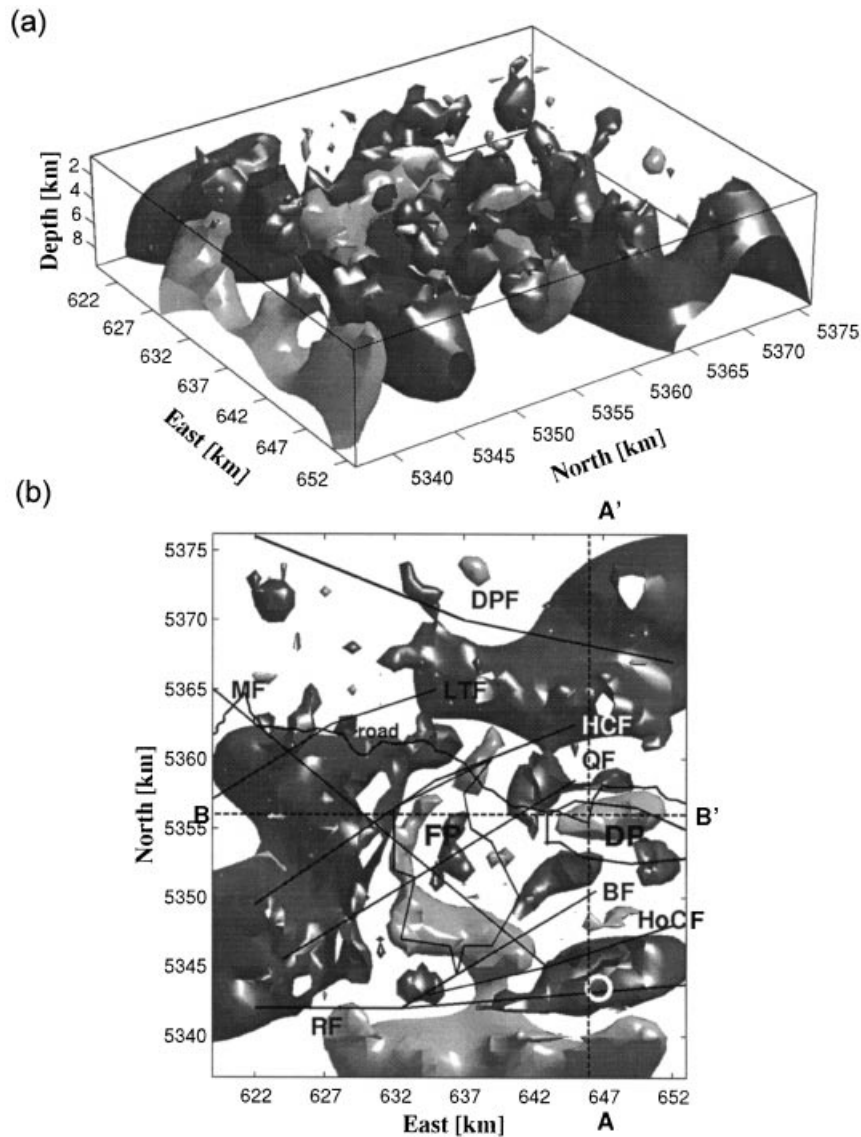


Figure 17 Isosurfaces of the 3D inversion results (lighting from the right) are presented in two different views: (a) looking from the SE with a vertical elevation of 30° and (b) from above. Pale and dark grey motifs correspond to density lower than 2.74 g/cm^3 and density higher than 2.85 g/cm^3 , respectively. Major faults (DPF, LTF, HCF, MF, QF, BF, HoCF, RF), the city of Rouyn (white circle), the Flavrian Pluton (FP) and the Dufault Pluton (DP) are drawn to help correlation. See Fig. 14 for legend of features.

distance as proposed by Green (1975) and formulated with a Lagrange function yields a flexible code which allows inclusion of flatness, smoothness and minimum volume constraints that can be used if needed. The code enables us to investigate different approaches to find an acceptable solution. Different powers for the depth weighting factor have been analysed to understand better the inverse reconstruction and to avoid concentration of the solution at the surface or at depth. In each case β must lie in the range $[0.5, 1]$. We suggest a standard selection of $\beta = 0.8$ for the

multigrid and $\beta = 0.9$ for the other constraints. The multigrid technique quickly yields a good approximation of the density structure, but it cannot be combined with other constraints. This is due to two factors: (i) inter-grid interpolation already includes a minimum volume constraint; (ii) the flatness constraint needs a sufficient number of cells to be efficient. Good density contrast can be obtained for each technique but the geometry is never recovered exactly. The best combination of constraints appears to be, at least for our study, flatness and minimum volume. By analysing the kernel, we

have found that sensitivity coefficients describe a symmetry with respect to the vertical z -axis. This symmetry allows efficient minimization of data storage. A simple analytical relationship has been derived from the kernel of spherical cells to assist in the choice of the discretization domain. The code needs only an estimate of the background density. Local constraints can be included by weighting particular cells. Density bounds can also be included to limit density contrast variations. Weighting, depending on a power of depth for each cell, is always recommended.

The basic solution is minimum distance. This method, in conjunction with the multigrid technique and the flatness constraint, can then improve the solution for the slowly varying densities often encountered in oil exploration. The method using the minimum volume constraint (compactness) is particularly suited to high density contrast, as is encountered in archaeological or geotechnical investigations for cavity detection. Flatness and minimum volume constraints can be the combination best suited for mineral exploration which seeks to detect a combination of high density contrasts for small bodies and low density contrasts for large bodies (background geology). When the number of parameters is large (e.g. greater than $100 \times 100 \times 40$ cells) the code becomes slow to run. Future work will include adaptive mesh refinement (AMR) in the inversion process to minimize the size of the matrix G and the time to run the forward problem. However, the program needs modest storage memory allowing it to run on a laptop computer. The code is written in C language and is available from the first author.

ACKNOWLEDGEMENTS

This work was supported by NSERC Strategic Grant STR0181406. We acknowledge Bruno Meurers (Associate Editor of GP in gravity and magnetism) and two anonymous referees for their valuable comments and suggestions.

REFERENCES

- Backus G. and Gilbert J.F. 1967. Numerical applications of a formalism for geophysical inverse problems. *Geophysical Journal of the Royal Astronomical Society* **13**, 247–276.
- Banerjee B. and Gupta S.P.D. 1977. Gravitational attraction of a rectangular parallelepiped. *Geophysics* **42**, 1053–1055.
- Barbosa V.C.F. and Silva J.B.C. 1994. Generalized compact gravity inversion. *Geophysics* **59**, 57–68.
- Bear G.W., Al-Shukri H.J. and Rudman A.J. 1995. Linear inversion of gravity data for 3-D density distributions. *Geophysics* **60**, 1354–1364.
- Bellefleur G. 1992. *Contribution of potential methods to the geological and the deep structure cartography in the Blake River Group, Abitibi*. MSc thesis, Ecole Polytechnique, Montreal (in French).
- Bhattacharyya B.K. and Leu L.-K. 1977. Spectral analysis of gravity and magnetic anomalies due to rectangular prismatic bodies. *Geophysics* **42**, 41–50.
- Briggs W. 1987. *A Multigrid Tutorial*. Society for Industrial and Applied Mathematics.
- Deschamps F., Chouteau M. and Dion D.-J. 1993. Geological interpretation of aeromagnetic and gravimetric data in the region located at the west part of the Rouyn-Noranda city. In: *Études Géophysiques Récentes de Certains Secteurs de la Ceinture Volcanosédimentaire de l'Abitibi* (ed. D.-J. Dion), Vol. DV 93-10 (ed. M. Germain), pp. 78–130. Ministère des Ressources Naturelles, Secteur des Mines (in French).
- Djeridane S. 1996. *Two-dimensional gravimetric inversion minimizing subsurface structures; application to Abitibi and Opatica sub-provinces*. MSc thesis, Ecole Polytechnique, Montreal (in French).
- Gauvin J. 1995. *Lessons of Mathematical Programming* Ecole Polytechnique, Montreal (in French).
- Gibson H. and Watkinson D. 1990. Volcanogenic massive sulphide deposits of the Noranda cauldron and shield volcano, Quebec. In: *Northwestern Quebec Polymetallic Belt*, Vol. 43 (eds M. Rive, P. Verpaelt, Y. Gagnon, J. Lulin, G. Riverin and A. Simard), pp. 119–132. Canadian Institute of Mining and Metallurgy.
- Golub G.H. and Van Loan C.F. 1996. *Matrix Computations*, 3rd edn. Johns Hopkins University Press.
- Green A., Milkereit B., Mayrand L., Ludden J., Hubert C., Jackson S. et al. 1990. Deep structure of an Archaean greenstone terrane. *Nature* **344**, 327–330.
- Green W.R. 1975. Inversion of gravity profiles by use of a Backus-Gilbert approach. *Geophysics* **40**, 763–772.
- Guillen A. and Menichetti V. 1984. Gravity and magnetic inversion with minimization of a specific functional. *Geophysics* **49**, 1354–1360.
- Haáz I.B. 1953. Relations between the potential of the attraction of the mass contained in a finite rectangular prism and its first and second derivatives. *Geofizikai Közlemények* **2** (7) (in Hungarian).
- Hackbusch W. and Trottenberg U. 1982. *Multigrid Methods*. Springer-Verlag, Inc.
- Jackson D. 1979. The use of a priori data to resolve non-uniqueness in linear inversion. *Geophysical Journal of the Royal Astronomical Society* **57**, 137–157.
- Jacobsen B.H. 1987. A case for upward continuation as a standard separation filter for potential-field maps. *Geophysics* **52**, 1138–1148.
- Keating P. 1992. Interpretation of the gravity anomaly field in the Noranda – Val d'Or region. Abitibi Greenstone Belt, Canadian Shield. *Canadian Journal of Earth Science* **29**, 962–971.
- Keating P. 1993. Interpretation of the gravity anomaly field in the Noranda – Val d'Or region. In: *Études Géophysiques Récentes de Certains Secteurs de la Ceinture Volcanosédimentaire de l'Abitibi* (ed. D.-J. Dion), Vol. DV 93-10 (ed. M. Germain), pp. 57–76. Ministère des Ressources Naturelles, Secteur des Mines (in French).
- Last B.J. and Kubik K. 1983. Compact gravity inversion. *Geophysics* **48**, 713–721.
- Li X. and Chouteau M. 1998. Three-dimensional gravity modelling in all space. *Surveys in Geophysics* **19**, 339–368.

- Li Y. and Oldenburg D.W. 1996. 3-D inversion of magnetic data. *Geophysics* **61**, 394–408.
- Li Y. and Oldenburg D.W. 1998. 3-D inversion of gravity data. *Geophysics* **63**, 109–119.
- Lines L.R. and Treitel S. 1984. Tutorial: A review of least-squares inversion and its application to geophysical problems. *Geophysical Prospecting* **32**, 159–186.
- Nagy D. 1966. The gravitational attraction of a right rectangular prism. *Geophysics* **31**, 362–371.
- Péloquin A., Potvin R., Paradis S., Laflèche M., Verpaelt P. and Gibson H. 1990. The Blake River Group, Rouyn-Noranda area, Québec: a stratigraphic synthesis. In: *Northwestern Québec Polymetallic Belt*, Vol. 43 (eds M. Rive, P. Verpaelt, Y. Gagnon, J. Lulin, G. Riverin and A. Simard), pp. 107–118. Canadian Institute of Mining and Metallurgy.
- Perron G. and Calvert A. 1998. Case history: Shallow, high-resolution seismic imaging at the Ansil mining camp in the Abitibi greenstone belt. *Geophysics* **63**, 379–391.
- Pilkington M. 1997. 3-D magnetic imaging using conjugate gradients. *Geophysics* **62**, 1132–1142.
- Verpaelt P., Péloquin A., Adam E., Barnes A., Ludden J., Dion D.-J. *et al.* 1995. Seismic reflection profiles across the 'Mines Series' in the Noranda camp of the Abitibi belt, eastern Canada. *Canadian Journal of Earth Science* **32**, 167–176.

APPENDIX A

Determination of the cell size to fit the gravity anomaly

There is a relationship between the cell size and the wavelength of the computed anomaly. The shortest wavelength observed in the data is obtained from the shallowest bodies. To analyse the sensitivity of the method with respect to the cell size used in computing the gravity effect, we search for the maximum size of a prism located in the top layer to fit the highest frequency (Nyquist frequency) displayed by the anomaly. The Fourier transform $F_g(u, v)$ of the gravity effect due to a prismatic body with a finite vertical extent can be formulated from Bhattacharyya and Leu (1977). If we take $u = 2\pi f_x$, $v = 2\pi f_y$, $s = \sqrt{u^2 + v^2}$, $h_1 = z'_1 - z_i$, $a = x'_2 - x'_1$, $b = y'_2 - y'_1$ and $c = z'_2 - z'_1$, then $F_g(u, v)$ is given by

$$F_g(u, v) = 16\pi\gamma\rho \frac{\sin\left(\frac{ua}{2}\right)}{u} \frac{\sin\left(\frac{vb}{2}\right)}{v} \frac{\sinh\left(\frac{sc}{2}\right)}{s} \times e^{-s\left(h_1 + \frac{c}{2}\right)} e^{-iu\left(x'_1 + \frac{a}{2}\right)} e^{-iv\left(y'_1 + \frac{b}{2}\right)}.$$

The Nyquist frequency of gravity data in the x -direction is

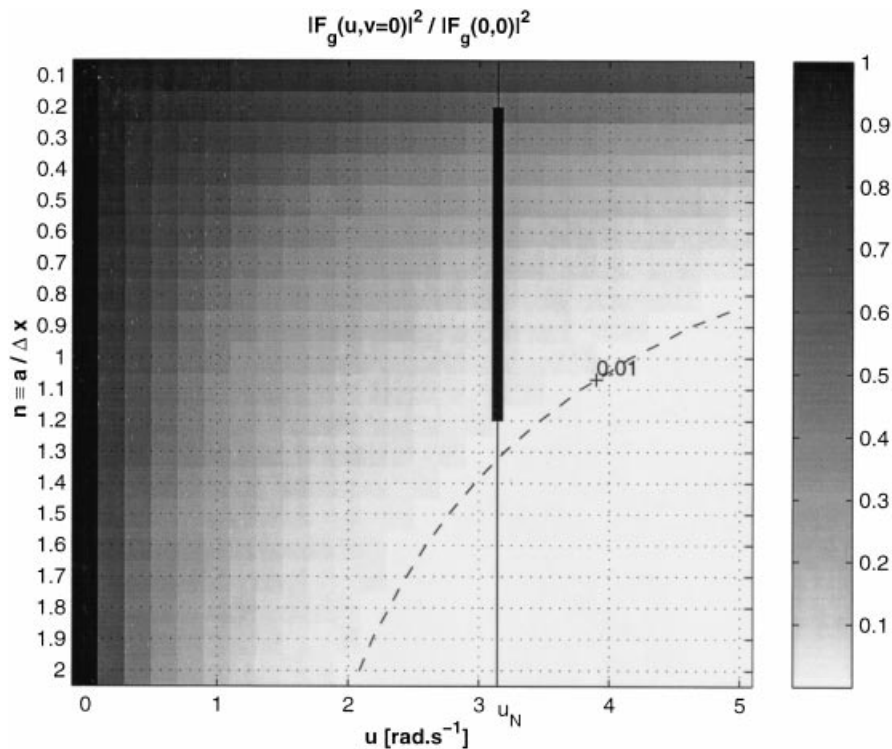


Figure 18 Normalized power spectra $\frac{|F_g(u, v=0)|^2}{|F_g(0, 0)|^2}$ in the direction u versus the ratio $n = \frac{a}{\Delta x}$. The fine line at u_N represents the highest frequency (Nyquist frequency) displayed by the gravity data. The thick line at u_N gives the range of $n = \frac{a}{\Delta x}$ for which the highest frequency in the gravity anomaly can be explained by a cell of size a at the surface. The dashed line corresponds to 1% of the normalized power spectra.

given by $f_N = \frac{1}{2\delta x}$. If we assume that $\delta x = 1$ and $a = b = c$, then $u_N = 2\pi f_N = \pi$. We can plot, for an observation at the surface (centre of top face with $h_1 = 0$), the normalized power spectra $\frac{|F_g(u, v=0)|^2}{|F_g(0, 0)|^2}$ in the direction u versus the ratio $n = \frac{a}{\delta x}$ (Fig. 18). The anomaly from the cubic cell will be able to reproduce the highest frequency in the data (Nyquist frequency) if the power at the Nyquist frequency is still large enough. We impose a threshold $\geq 1\%$ of normalized power ($\geq 10\%$ of normalized amplitude) as a minimum bound to fulfil this condition. From Fig. 18, it can be concluded that cells with a size $\frac{a}{\delta x} \leq 1.2$ are needed. In all cases presented in this paper, we use $a = \delta x$. The same reasoning is valid for δy .

APPENDIX B

Multigrid technique

Gravity observations are sampled in the x - and y -directions for solving first long anomaly wavelengths and then short wavelengths. We need to do this in order to decompose the observation set into several levels. The first level is the finest, composed of all data, and the last one is the coarsest. These levels can be run in different ways by designing a cycle (Nested N-cycle, V-cycle, W-cycle, Full Multigrid FMV-cycle and FMVI-cycle) shown in Fig. 19. When the inter-grid transfer of density ρ_j moves from a fine grid δ^i to a coarse grid δ^{i+1} , denoted by $R = I_{\delta^i}^{\delta^{i+1}}$, it is called *restriction* (or injection). A *prolongation* is performed by the operator, $P = I_{\delta^{i+1}}^{\delta^i}$ for an interpolation from level δ^{i+1} to level δ^i . We use here a simple tri-linear interpolation I of ρ_j weighted by \mathcal{V}_{jj}^{-1} , defined in the section 'Formulation', to obtain a better result. Because two successive level grids do not coincide but overlap each other, we need to define a neighbourhood around each cell ρ_j during the inter-grid transfer of the density to avoid a density smoothing. Thus, the limits of interpolation at a point \mathbf{x} in the space for prolongation and restriction are defined as $\rho_j^{\delta^{i+1}}(\mathbf{x} - \nu\delta^i) \leq \rho_j^{\delta^i}(\mathbf{x})\mathcal{V}_{jj}^{-1} \leq \rho_j^{\delta^{i+1}}(\mathbf{x} + \nu\delta^i)$

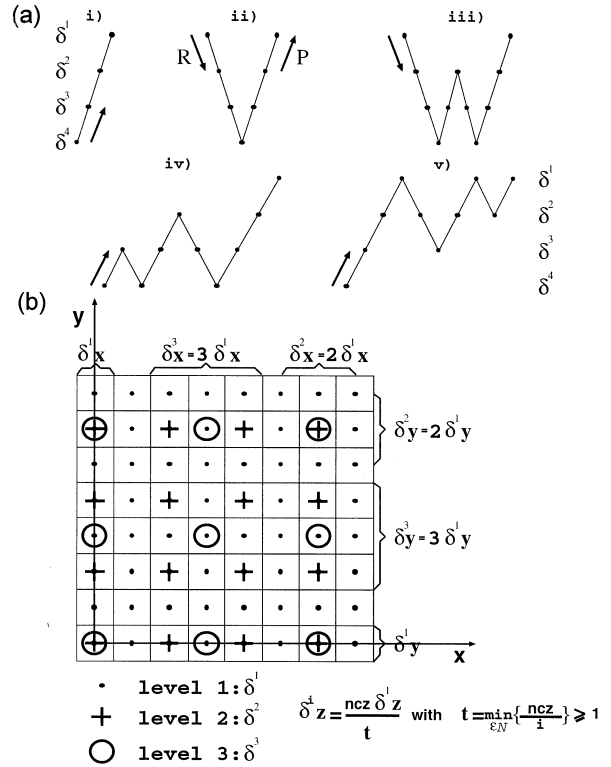


Figure 19 (a) Types of cycle with restriction ($R = I_{\delta^i}^{\delta^{i+1}}$) and prolongation ($P = I_{\delta^{i+1}}^{\delta^i}$): (i) Nested, (ii) V-cycle, (iii) W-cycle, (iv) FMV-cycle, (v) FMVI-cycle. (b) Discretization in all directions and sampling of data (\bullet , $+$, \circ) for each level $i = 1, 2, 3$ (δ^i).

and $\rho_j^{\delta^i}(\mathbf{x} - \nu\delta^{i+1}) \leq \rho_j^{\delta^{i+1}}(\mathbf{x})\mathcal{V}_{jj}^{-1} \leq \rho_j^{\delta^i}(\mathbf{x} + \nu\delta^{i+1})$, respectively (where $\nu = 0.5$ only for prolongation in the z -direction, otherwise $\nu = 1$). Increments of the grid for each level in the x - and y -directions are calculated as $\delta^i = i\delta^1$, and for the z -direction as $\delta_z^i = \frac{ncz\delta^1}{t}$ where $t = \{\frac{ncz}{1}\} \geq 1$ is an integer value ($t \in \mathbb{N}$). We calculate the Jacobian matrix \mathbf{G}^{δ^i} depending on the increments δ^i in the x -, y - and z -directions, and solve the system of equations (11) (with $\mathbf{A} \equiv \mathbf{G}^{\delta^i}$) with the same global rms tolerance at each level i .